The Astrophysical Journal, 947:44 (10pp), 2023 April 20 https://doi.org/10.3847/1538-4357/acc6c2

SPT-CL J2215−3537: A Massive Starburst at the Center of the Most Distant Relaxed Galaxy Cluster

Michael S. Calzadilla[1], Lindsey E. Bleem[2,3], Michael McDonald[1], Michael D. Gladders[3,4], Adam B. Mantz[5], Steven W. Allen[5], Matthew B. Bayliss[6], Anna-Christina Eilers[1], Benjamin Floyd[7], Julie Hlavacek-Larrondo[8], Gourav Khullar[9], Keunho J. Kim[6], Guillaume Mahler[10,11], Keren Sharon[12], Taweewat Somboonpanyakul[5], Brian Stalder[13], and Antony A. Stark[13]
(SPT collaboration)

[1] Kavli Institute for Astrophysics and Space Research, Massachusetts Institute of Technology, Cambridge, MA 02139, USA; msc92@mit.edu
[2] High Energy Physics Division, Argonne National Laboratory, 9700 South Cass Avenue, Argonne, IL 60439, USA
[3] Kavli Institute for Cosmological Physics, University of Chicago, 5640 South Ellis Avenue, Chicago, IL 60637, USA
[4] Department of Astronomy and Astrophysics, University of Chicago, 5640 South Ellis Avenue, Chicago, IL 60637, USA
[5] Kavli Institute for Particle Astrophysics and Cosmology, Stanford University, 452 Lomita Mall, Stanford, CA 94305, USA
[6] Department of Physics, University of Cincinnati, Cincinnati, OH 45221, USA
[7] Faculty of Physics and Astronomy, University of Missouri–Kansas City, 5110 Rockhill Road, Kansas City, MO 64110, USA
[8] Département de Physique, Université de Montréal, Succ. Centre-Ville, Montréal, Québec, H3C 3J7, Canada
[9] Department of Physics and Astronomy and PITT PACC, University of Pittsburgh, Pittsburgh, PA 15260, USA
[10] Centre for Extragalactic Astronomy, Durham University, South Road, Durham DH1 3LE, UK
[11] Institute for Computational Cosmology, Durham University, South Road, Durham DH1 3LE, UK
[12] Department of Astronomy, University of Michigan, 1085 South University Avenue, Ann Arbor, MI 48109, USA
[13] Center for Astrophysics | Harvard & Smithsonian, 60 Garden Street, Cambridge, MA 02138, USA
Received 2022 November 3; revised 2023 March 13; accepted 2023 March 16; published 2023 April 19

Abstract

We present the discovery of the most distant, dynamically relaxed cool core cluster, SPT-CL J2215−3537 (SPT2215), and its central brightest cluster galaxy (BCG) at $z = 1.16$. Using new X-ray observations, we demonstrate that SPT2215 harbors a strong cool core with a central cooling time of 200 Myr (at 10 kpc) and a maximal intracluster medium cooling rate of $1900 \pm 400\ M_{\odot}\ \mathrm{yr}^{-1}$. This prodigious cooling may be responsible for fueling the extended, star-forming filaments observed in Hubble Space Telescope imaging. Based on new spectrophotometric data, we detect bright [O II] emission in the BCG, implying an unobscured star formation rate (SFR) of $320^{+230}_{-140}\ M_{\odot}\ \mathrm{yr}^{-1}$. The detection of a weak radio source (2.0 ± 0.8 mJy at 0.8 GHz) suggests ongoing feedback from an active galactic nucleus (AGN), though the implied jet power is less than half the cooling luminosity of the hot gas, consistent with cooling overpowering heating. The extreme cooling and SFR of SPT2215 are rare among known cool core clusters, and it is even more remarkable that we observe these at such high redshift, when most clusters are still dynamically disturbed. The high mass of this cluster, coupled with the fact that it is dynamically relaxed with a highly isolated BCG, suggests that it is an exceptionally rare system that must have formed very rapidly in the early universe. Combined with the high SFR, SPT2215 may be a high-z analog of the Phoenix cluster, potentially providing insight into the limits of AGN feedback and star formation in the most massive galaxies.

Unified Astronomy Thesaurus concepts: Galaxy clusters (584); High-redshift galaxy clusters (2007); Starburst galaxies (1570); Star formation (1569); Intracluster medium (858); Cooling flows (2028)

1. Introduction

Galaxy clusters are rich collections of hundreds to thousands of galaxies. However, most of the luminous mass in a cluster is found in a hot ($T \sim 10^7$ K) X-ray-emitting phase that permeates the space between these galaxies. This vast X-ray-emitting plasma is called the intracluster medium (ICM). As this ICM cools over time, it releases energy via bremsstrahlung radiation and falls deeper into the gravitational potential well of the cluster. This cooling steepens the density profile of the cluster, which allows for more frequent interactions within the plasma and further decreases the temperature in the center, leading to what is referred to as a "cool core" (CC) cluster (e.g., Hudson et al. 2010).

At the center of a CC cluster, there is usually one dominant brightest cluster galaxy (BCG) onto which the cooling flow from the ICM is deposited. In the absence of any heat input, these BCGs are expected to vigorously form stars and contain large reservoirs of molecular gas (see review by Fabian 1994). Instead, observations of large samples of these systems show very little of either, with cooling suppressed, on average, by 2 orders of magnitude compared to theoretical predictions (e.g., Johnstone et al. 1987; McNamara & O'Connell 1989; Allen 1995; Crawford et al. 1999; Rafferty et al. 2006; O'Dea et al. 2008; Donahue et al. 2015; McDonald et al. 2018). The cooling funneled onto the BCG also makes its way to its central active galactic nucleus (AGN), where accretion onto a supermassive black hole (SMBH) leads to massive outbursts in the form of relativistic outflows of plasma, which in turn deposit heat into the ICM. Such "feedback" in response to feeding establishes the central SMBH as a sort of thermostat that regulates the temperature and the amount of cool gas

available for forming stars (see reviews by McNamara & Nulsen 2007; Fabian 2012; McNamara & Nulsen 2012; Gaspari et al. 2020; Donahue & Voit 2022). In nearby clusters, this behavior seems tightly regulated (e.g., Hlavacek-Larrondo et al. 2015). We know much less about the behavior of feedback and cooling at higher redshifts, when clusters are still in the process of virializing and the availability of gas and the rate of cosmic star formation were much higher.

Studies of large samples of high-redshift clusters have been enabled by Sunyaev–Zel'dovich (SZ) effect-based surveys (e.g., Vanderlinde et al. 2010; Bleem et al. 2015; Planck Collaboration et al. 2016; Hilton et al. 2021) and, more recently, by more sensitive X-ray survey telescopes like eROSITA (Liu et al. 2022). The SZ surveys have discovered many more galaxy clusters in a mass-limited way, which allows us to study the balance between AGN feedback and ICM cooling over cosmic history (e.g., McDonald et al. 2013). Among the new lessons learned is that this feedback cycle has been in place for at least $\sim$10 Gyr (Hlavacek-Larrondo et al. 2015; Ruppin et al. 2022). The fraction of CCs in clusters has also remained constant with redshift (McDonald et al. 2013, 2017; Ruppin et al. 2021). One might expect different behaviors at early times, as clusters are still rapidly forming and accreting subhalos, and the average galaxy is more likely to be both star-forming and hosting an AGN (e.g., Hlavacek-Larrondo et al. 2013; Somboonpanyakul et al. 2022). One possible example of this is SpARCS 104922.6+564032.5 (SpARCS1049; $z = 1.7$), which hosts a starburst that is not centered on any galaxy, i.e., in the absence of AGN feedback (Webb et al. 2015; Hlavacek-Larrondo et al. 2020). Over time, such a cooling flow may be quenched by the eventual alignment of the cluster potential between the BCG and AGN due to dynamical friction.

In this work, we present the first detailed study of the massive ($M_{500c} = 7.32 \times 10^{14}\ M_{\odot}$) high-redshift ($z = 1.16$) galaxy cluster SPT-CL J2215−3537 (SPT2215). This cluster was discovered in the SPTpol Extended Cluster Survey (Bleem et al. 2020) and is among the most massive clusters known at $z > 1$. Based on Chandra imaging, Mantz et al. (2022) determined SPT2215 to be dynamically relaxed, and it was considered as part of a larger sample of relaxed clusters in order to provide tighter constraints on the cosmological parameters. This study focuses on some of the extraordinary properties of SPT2215 in more detail. In Section 2, we describe multiwavelength follow-up observations of this system and how these were reduced. In Section 3, we lay out the extreme qualities of this cluster, namely, how isolated, relaxed, and star-forming the central galaxy is. Finally, we discuss the importance of this cluster in a cosmological context in Section 4 before summarizing in Section 5. Throughout this paper, we assume a flat ΛCDM cosmology with $H_0 = 70$ km s^{-1} Mpc^{-1}, $\Omega_m = 0.3$, and $\Omega_\Lambda = 0.7$. This yields a physical scale of 8.25 kpc arcsec^{-1} at the redshift of the cluster. All measurement errors are 1σ unless noted otherwise.

2. Observations and Data Reduction

2.1. X-Ray (Chandra)

Chandra observations of SPT2215 were taken as part of a follow-up X-ray campaign of SPT SZ-selected clusters. The observations presented here were taken with the ACIS-I instrument for a total of 72.26 ks (ObsIDs 22653, 24614, and 24615; PI: McDonald). These data were reduced and analyzed using the Chandra Interactive Analysis of Observations (CIAO) v4.12.1 software with CALDB v4.9.2 in a standard fashion similar to McDonald et al. (2013), Calzadilla et al. (2019), and Ruppin et al. (2021, 2022). The latest gain and charge transfer inefficiency corrections were applied, with improved background screening for the VFAINT telemetry mode. Modeling of the global ICM properties was done as in Calzadilla et al. (2022), and the thermodynamic profiles are shown and discussed in Section 3.1.

To model the emission of the optically thin, X-ray-emitting plasma in this cluster, we use the APEC/AtomDB XSPEC v3.0.9 thermal spectral model (Smith et al. 2001), in addition to PHABS for photoelectric absorption (Morrison & McCammon 1983). We adopt Anders & Grevesse (1989) abundances for consistency with previous literature and hydrogen column density $N_{\rm H} = 1.07 \times 10^{20}$ cm^{-2} from the Leiden–Argentine–Bonn survey (Kalberla et al. 2005).

2.2. Optical Spectroscopy

As part of an ongoing follow-up campaign of SZ-selected clusters (e.g., Bayliss et al. 2016; Khullar et al. 2019, 2022), the SPT collaboration gathered optical spectroscopy of SPT2215 with the LDSS3 instrument on the 6.5 m Magellan telescopes in Chile. Multiobject spectra were obtained on 2019 June 25 using 1.″3 slits placed on the BCG and 16 other high-redshift member galaxy candidates. Observations were made over seven exposures totaling 2.3 hr of LDSS3 spectroscopy with the VPH-Red grism (1.175 Å pixel^{-1} dispersion) and open filter, bracketed by flat and comparison HeNeAr arc frames. The science and arc exposures were bias- and flat-field-corrected using pyRAF/IRAF,[14] specifically with the imred.ccdred package. We also use the response task from twodspec.longslit to fit for the shape of the lamp spectrum in the dispersion direction before flat-fielding. In the resulting reduced science frames, we identify the BCG spectrum of SPT2215 and trace the slit using the twodspec package apall to extract a one-dimensional (1D) spectrum with background subtraction. The same traced apertures were used to extract 1D spectra from the arc frames, which where then used to find a wavelength calibration solution with the identify task. The onedspec refspec and dispcor tasks were then used to assign and apply the wavelength solution to the science frames. Each of the wavelength-calibrated science frames was then median-combined with cosmic-ray rejection using scombine to produce a final 1D spectrum of the BCG with a wavelength range of $\lambda = [6800, 10500]$ Å and dispersion of 2 Å pixel^{-1}.

2.3. Optical/UV Imaging and Photometry

2.3.1. Hubble Space Telescope ACS/WFC3

Object SPT2215 was imaged as part of the Hubble Space Telescope (HST) Cycle 25, 26 HST-SNAP program (GO-15307, GO-16017; PI: Gladders). Observations were obtained on UT 2017 October 6 with the Wide Field Camera 3 (WFC3) using the F110W (984 s) and F200LP (817 s) filters. The F110W and F200LP filters sample the rest-frame emission from about 4170–6480 and 925–4600 Å, respectively. Special

[14] https://iraf-community.github.io/pyraf.html

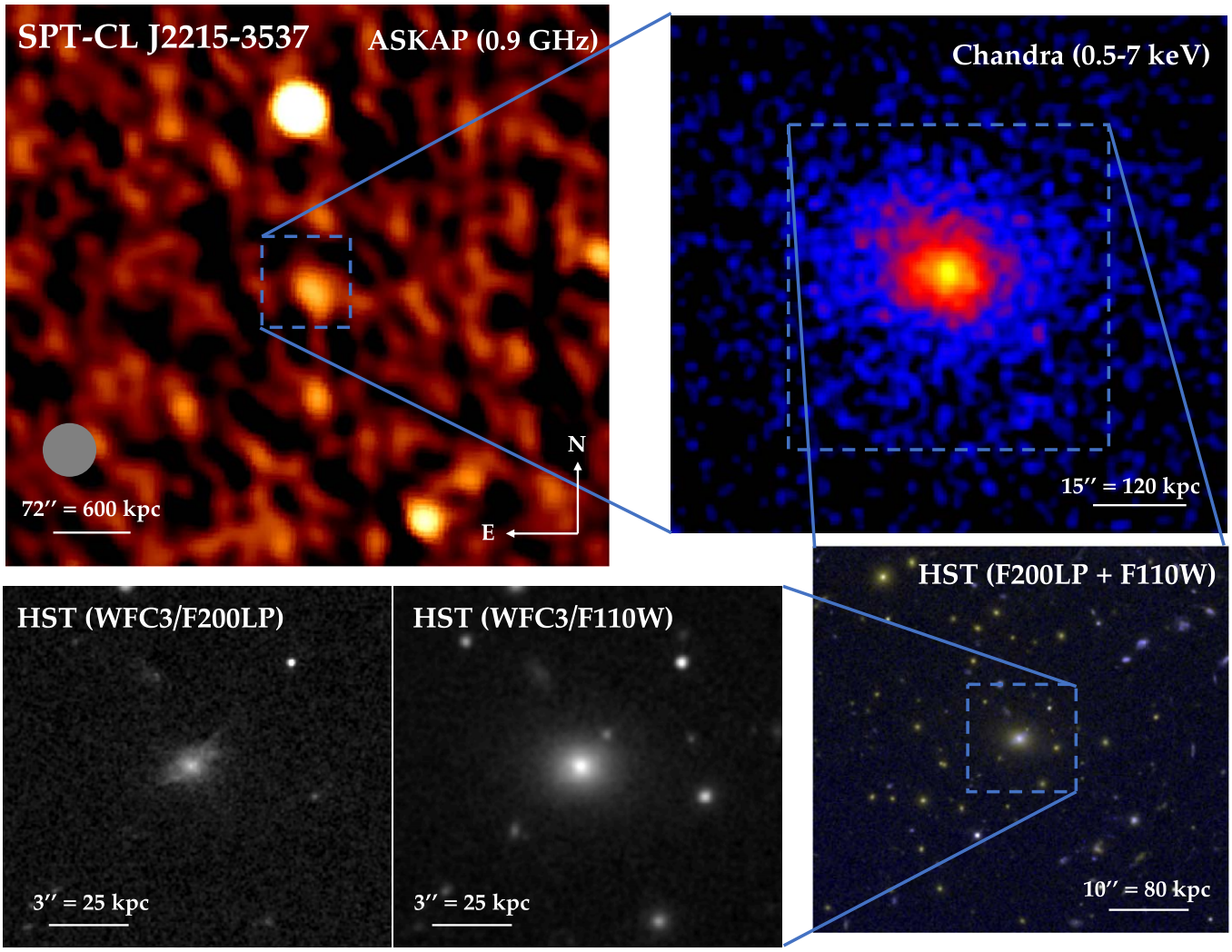

Figure 1. Multiwavelength observations of SPT2215, progressively zooming in clockwise through the images. Top left: ASKAP 887 MHz radio image cutout showing the presence of a radio source/AGN with an integrated flux of 2.0 ± 0.8 mJy at 0.8 GHz. The ASKAP beam size is shown in gray. Top right: 0.5–7 keV Chandra X-ray image showing a very relaxed ICM morphology and a strongly peaked central surface brightness profile. Bottom right: two-band HST composite image of the cluster, with zoomed-in views of the central BCG in the bottom middle (HST WFC3/F110W) and bottom left (HST WFC3/F200LP) panels. The bluer F200LP observation shows the presence of extended blue filaments that likely indicate strong star formation fueled by cooling out of the hot ICM.

care had to be taken in the reduction of the F110W data to generate an appropriately flat-fielded image reducing the effects of known "IR blobs," which are small regions where detector sensitivity is lowered by 10%–15%. These features were modeled out by analyzing the stacked images of hundreds of similar-exposure observations from the archive. After this, the observations were processed in a standard way using STScI's `DrizzlePac` software package[15] with `AstroDrizzle (v3.3.1)`. Observations from both filters were combined and drizzled to the same pixel grid, with a resulting resolution of $0\farcs3$ pixel^{-1}. All of the HST data used in this paper can be found in MAST doi:10.17909/pr0c-c679.

2.3.2. Magellan PISCO

Optical imaging of SPT2215 was obtained for 300 s in $1\farcs2$ seeing on 2017 June 22 in the *griz* bands using the Parallel Imager for Southern Cosmology Observations (PISCO; Stalder et al. 2014) installed on the 6.5 m Magellan Clay Telescope. The image reduction process is detailed in Bleem et al. (2020). Sources were extracted using SExtractor (Bertin & Arnouts 1996), star–galaxy separation was performed using the SG statistic (Bleem et al. 2015), and photometric calibration was performed using stellar locus regression (SLR) techniques (High et al. 2009). PISCO astrometry was tied to stars from the Dark Energy Survey public data release (Abbott et al. 2018).

2.3.3. Magellan FourStar

To complement the optical imaging, 640 s of *J*- and *H*-band near-infrared imaging with the Magellan FourStar (Persson et al. 2013) was obtained on 2017 October 2. As detailed in Bleem et al. (2020), the images were flat-fielded with IRAF routines and astrometrically registered and relatively calibrated using the PHOTPIPE pipeline (e.g., Miknaitis et al. 2007). Absolute photometric calibration was undertaken using SLR. Astrometry was tied to the Two Micron All Sky Survey (2MASS) catalog (Skrutskie et al. 2006).

[15] https://drizzlepac.readthedocs.io/en/latest/

2.3.4. Spitzer IRAC

Spitzer IRAC observations at 3.6 (I1) and 4.5 μm (I2) of SPT2215 were obtained as part of a follow-up program to identify galaxy counterparts for high-redshift massive SZ cluster candidates (PID 11096; PI: Bleem). The cluster was observed for 360 s of on-source time in both bands; the data were reduced and photometered following the methodology detailed in Ashby et al. (2009). Astrometry was also tied to the 2MASS catalog.

3. Analysis and Results

3.1. The Most Distant Relaxed CC Cluster

As mentioned before, SPT2215 was previously determined to be dynamically relaxed in Mantz et al. (2022). This was done by characterizing the morphology of the X-ray-emitting ICM, which looks largely spherically symmetric, as seen in the Chandra image in the top right panel of Figure 1. More quantitatively, using the ICM symmetry, peakiness, and isophotal alignment (SPA) criteria from Mantz et al. (2015) to determine the degree of relaxedness, these measurements yield $S = 1.24 \pm 0.15$, $P = -0.46 \pm 0.04$, and $A = 1.42 \pm 0.16$ (Mantz et al. 2022). In Figure 2, we compare the SPA measurements of SPT2215 to the sample of clusters from Mantz et al. (2015), who identified thresholds that separate relaxed and disturbed clusters. We see that the SPA measurements for SPT2215 indeed lie firmly in the relaxed locus in this parameter space.

The dynamical state of this cluster can be further validated by looking at the optical HST images shown in Figure 1 (bottom panels), which indicate that the BCG at the center of the frame is exceptionally bright, with an extended diffuse envelope of light. There are no other galaxies out to $\sim$200 kpc in projected distance that appear nearly as bright or extended. We only consider this distance in order to minimize contamination from foreground or background galaxies not associated with the cluster. Within this radius, we measure background-subtracted F110W fluxes from $\sim$10 kpc radius circular apertures centered on the brightest neighboring galaxies and compare to that of the BCG. The smallest magnitude gap, corresponding to the flux ratio between the BCG and the second brightest galaxy (e.g., Milosavljević et al. 2006; van den Bosch et al. 2007), is $\Delta M_{1,2} \approx 2.2 \pm 0.1$. In the literature, systems with R-band gaps of $\Delta M_{1,2} \gtrsim 1.7$ are classified as fossil groups (e.g., Jones et al. 2003) and thought to be old, undisturbed systems that have not experienced a significant recent merger (D'Onghia et al. 2005). The large magnitude gap observed here suggests that SPT2215 has not recently experienced a significant merger, which is consistent with the exceptionally relaxed X-ray morphology.

In addition to the morphological analyses above, we conduct a spectroscopic analysis of the X-ray data to determine the thermodynamic properties of the ICM as a function of radius. We extract spectra from both coarse and fine annular bins centered on the BCG ($\alpha = 22^{\rm h}15^{\rm m}03\overset{\rm s}{.}9306$, $\delta = -35°37'17\overset{''}{.}885$). The coarse bins are used to fit a PHABS*APEC model with fixed metallicity ($Z = 0.3\ Z_{\odot}$) in order to measure the ICM temperature. We use a Vikhlinin et al. (2006) parametric model,

$$T_{\rm 3D}(r) = T_0 \frac{(r/r_{\rm cool})^{\alpha} + T_{\rm min}/T_0}{(r/r_{\rm cool})^{\alpha} + 1} \frac{(r/r_{\rm t})^{a}}{[1 + (r/r_{\rm t})^{b}]^{c/b}}, \quad (1)$$

where a, b, and c model the outer regions of the profile with a flexible broken power law. The profile falls off at large radii at around r_t, while the inner CC region is defined by T_0, $T_{\rm min}$, $r_{\rm cool}$, and α. This 3D temperature profile is projected along the line of sight and fit to the extracted coarse temperature profile in projection. To quantify the uncertainty in our best-fit model, we perform our fits over 100 Monte Carlo simulations that sample the data points within their errors, assuming Gaussianity. As we only extract four spectroscopic temperature measurements, we freeze a number of parameters in our fits to be able to reliably constrain our temperature model. In all Monte Carlo iterations, we set $a = 0$ and $\alpha = 2$, while the parameters b, c, and T_0 are each randomly sampled in each iteration from the distribution of values found in Vikhlinin et al. (2006, Table 3) and subsequently fixed. Additionally, $T_{\rm min}$ is fixed to the innermost randomly sampled temperature value for any given Monte Carlo iteration. The best temperature fit is interpolated at the same radii as the fine annular binning scheme described before, for which we again extract spectra and fit them with the same model. For these finer spectral fits, we fix the interpolated temperature values and allow only the APEC model normalization to vary. These normalizations per unit area can be converted to an emission measure (EM) profile, to which we fit a projected Vikhlinin et al. (2006) EM model,

$$n_{\rm e} n_{\rm p}(r) = n_0^2 \frac{(r/r_{\rm c})^{-\alpha}}{[1 + (r/r_{\rm c})^2]^{3\beta - \alpha/2}} \frac{1}{[1 + (r/r_{\rm s})^{\gamma}]^{\epsilon/\gamma}} + \frac{n_{02}^2}{[1 + (r/r_{\rm c2})^2]^{3\beta_2}}, \quad (2)$$

which is a modified double-beta model with a cusp rather than a flat core (defined by n_0, $r_{\rm c}$, α, and β), a steeper outer profile slope (defined by $r_{\rm s}$, γ, and ϵ), and a CC component (defined by n_{02}, $r_{\rm c2}$, and β_2). Here n_e and n_p correspond to the electron and proton number densities, respectively. In our fits, $\gamma = 3$ and $\epsilon = 5$ remain fixed, and all other parameters are allowed to vary and initialized to the typical parameters found in Vikhlinin et al. (2006, Table 2). These fits to the temperature and EM profiles are performed over 100 Monte Carlo realizations in order to get uncertainty regions for the corresponding profiles by sampling data points to fit from their measured uncertainties (assuming Gaussianity).

The resulting best-fit EM and temperature profiles can be found in Figure 3. After obtaining the density (n_e) profile from the (unprojected) EM profile, we combine these individual profiles to produce unprojected (3D) pseudo-entropy ($k_B T n_e^{-2/3}$) and cooling time profiles ($t_{\rm cool} = \frac{(n_e + n_p) k_B T}{n_e n_p \Lambda(k_B T, Z)}$). We use the cooling function $\Lambda(k_{\rm B}T, Z)$ from Sutherland & Dopita (1993) as parameterized by Tozzi & Norman (2001). Given the central temperature drop (a factor of $\sim$3×) and increase in density, we determine that this cluster does in fact contain a CC. At a radius of 10 kpc, the central entropy and cooling time reach $\sim$20 keV cm^2 and 200 Myr, respectively. There are also a number of diagnostic criteria that predict where multiphase cooling out of the ICM ensues. For instance, Cavagnolo et al. (2008) were among the first to find a central entropy threshold in the cores of galaxy clusters of $K = 30$ keV cm^2 or, equivalently, where $t_{\rm cool} \approx 1$ Gyr, below which strong Hα and radio emission can be detected. For SPT2215, the cooling time profile drops below 1 Gyr at a radius of roughly 60 kpc, and the entropy drops below 30 keV cm^2 at a

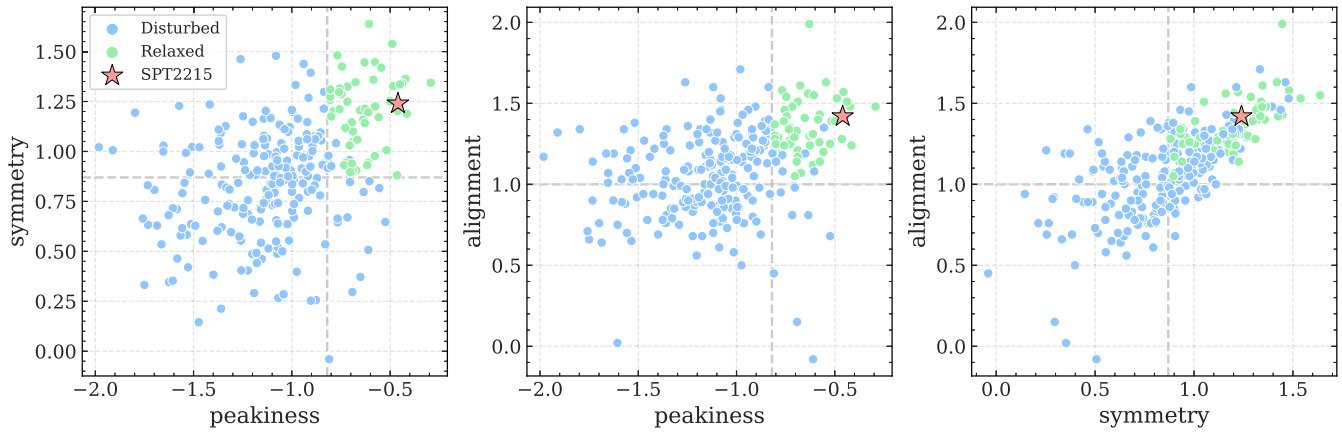

Figure 2. The SPA relaxedness criteria based on the symmetry (S), peakiness (P), and isophotal alignment (A) of ICM X-ray morphology for a sample of clusters (adapted from Mantz et al. 2015). Combined 3D cuts along each of these axes separate the clusters into those that are dynamically relaxed (green circles) and unrelaxed (blue circles). Object SPT2215 is plotted as a red star and can be seen to pass the above cuts, distinguishing it as a relaxed cluster.

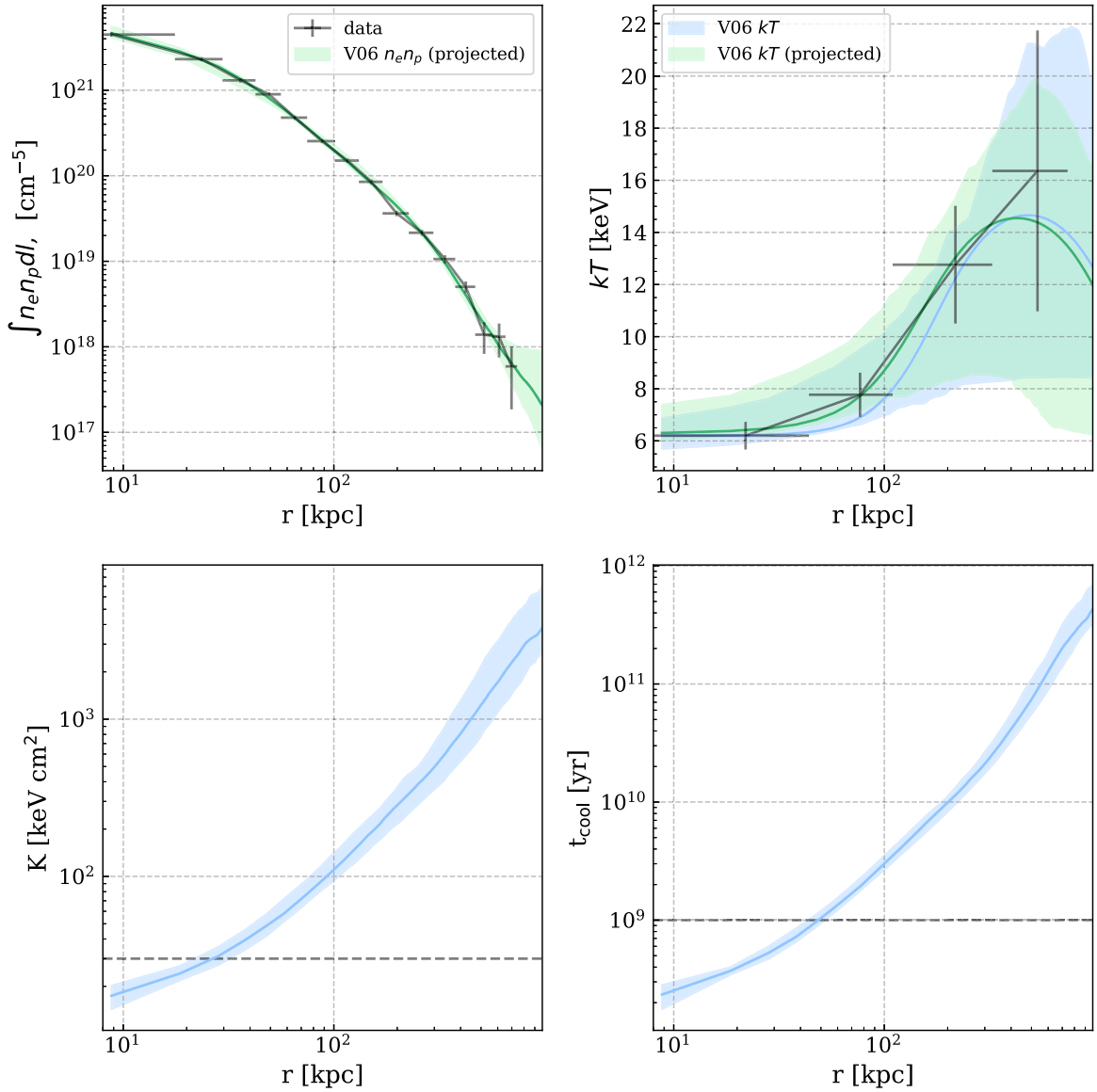

Figure 3. The ICM thermodynamic profiles for SPT2215. Top left: EM. Top right: temperature (k_{BT}) in units of keV. Bottom left: pseudo-entropy in units of keV cm^2. Bottom right: cooling time in years. In the top panels, green shaded regions represent EM and temperature models from Vikhlinin et al. (2006, Equations (3) and (6), respectively) that have been projected along the line of sight and fit to the data that were sampled via the Monte Carlo method. The corresponding unprojected (3D) models in all panels are shown as blue shaded regions. In the bottom panels, a horizontal dashed line marks the entropy ($K < 30$ keV cm^2) and cooling time ($t_{cool} < 1$ Gyr) CC thresholds below which we expect to see multiphase cooling, star formation, and AGN activity (e.g., Cavagnolo et al. 2008).

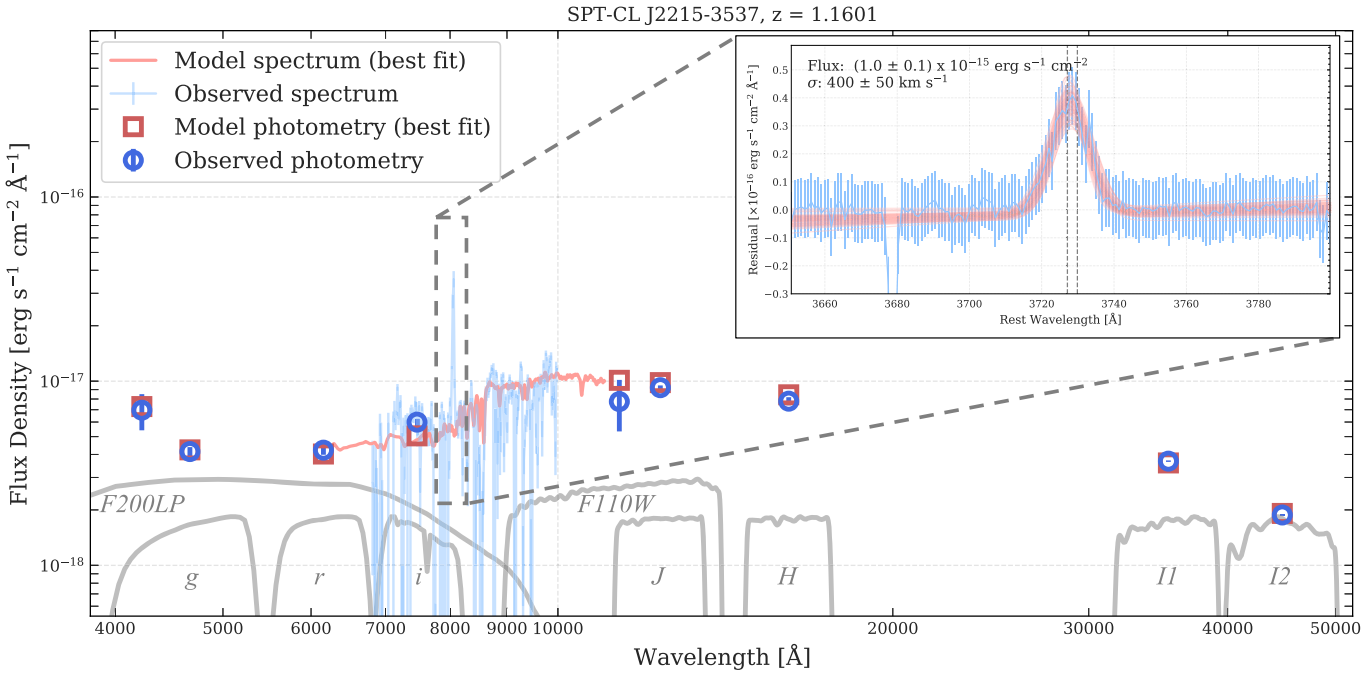

Figure 4. Observed SED for the BCG in SPT2215, including the flux-calibrated spectrum (light blue) and optical photometry (dark blue circles) from the PISCO *gri* and F200LP and F110W HST bands. Additional IR photometry in the FourStar *JH* and Spitzer I1 (3.6 μm) and I2 (4.5 μm) bands was also included in the SED fitting in order to better constrain the BCG stellar mass. The best-fit model spectrum obtained with the `prospector` SED fitting software is shown in light red, with the best-fit model photometry shown as dark red squares. The input spectrum was flux calibrated using the observed photometry to fit for the shape of the spectrum as a nuisance parameter and binned by 30 Å here for clarity. In the inset, we show the unbinned, residual rest-frame spectrum after subtracting the best-fit stellar continuum, zooming in on the spectral region surrounding strong [O II] emission. We fit this emission to measure an obscured flux of $\sim 1 \times 10^{-15}$ erg s^{-1} cm^{-2}, which implies an unobscured SFR of 320^{+230}_{-140} $M_\odot$ yr^{-1}. In the rest frame, the doublet location is consistent with the stellar continuum redshift (vertical dashed lines) and has an instrumental broadening-corrected width of 400 ± 50 km s^{-1}, which could indicate the presence of a strong wind most likely powered by the massive ongoing starburst.

radius of roughly 30 kpc. Having met these criteria, we might expect a large amount of cooling multiphase gas to condense and cool out of the hot X-ray-emitting phase. As an upper limit to the amount of material that can cool, we calculate a maximal cooling rate of $\dot{M}_{\rm cool} \equiv M_{\rm gas}(r < r_{\rm cool})/t_{\rm cool}(r = r_{\rm cool}) = 1900 \pm 400$ $M_\odot$ yr^{-1} by dividing the gas mass within some cooling radius by the cooling time at that cooling radius. Here we choose $r_{\rm cool} = 116 \pm 15$ kpc as the radius where the cooling time is $t_{\rm cool} = 3$ Gyr to probe cooling closer to the core and for ease of comparison to literature $\dot{M}_{\rm cool}$ values. This high cooling rate puts SPT2215 in an extreme part of parameter space that only a handful of other clusters occupy (e.g., Phoenix and RBS797; McDonald et al. 2018).

3.2. An Extremely High SFR

Given the extreme cooling rate implied by the Chandra X-ray data described in Section 3.1, we may also expect this condensation to fuel a large amount of star formation. Zooming in on the central BCG, we see in the bottom left panel of Figure 1 a network of filaments in the F200LP filter, which probes rest-frame emission blueward of ~4300 Å. These filaments reach a maximum projected extent of ~20 kpc, though deeper observations could reveal more emission further out. Filamentary nebulae like these typically signal regions of ionization by young stars and can be seen in many other strong cooling clusters (e.g., McDonald et al. 2010; Calzadilla et al. 2022). This observation utilizes a very broad F200LP filter that includes a large amount of rest-frame UV continuum, so we only use it here for an approximate estimate of the UV-derived star formation rate (SFR). By measuring the flux from a circular aperture ($2\farcs5 \approx 20$ kpc in radius) centered on the BCG, we measure a UV luminosity of $(3.7 \pm 0.3) \times 10^{29}$ erg s^{-1} Hz^{-1}. This luminosity can be converted to an SFR using the Rosa-González et al. (2002) relation, which is calibrated to account for any intrinsic extinction when it is not possible to measure it directly. With this relation, we calculate an SFR of $\sim 240 \pm 20$ $M_\odot$ yr^{-1}.

The high resolution but shallow HST imaging data in Figure 1 are complemented by ground-based imaging and spectroscopy using the Magellan 6.5 m telescopes. In particular, our LDSS3 spectroscopic observations for this cluster are especially helpful in securing an independent optical SFR estimate, as well as a precise redshift. The wavelength-calibrated spectrum obtained from the reduction steps outlined in Section 2.2 was fit in combination with optical *gri* photometry from PISCO and the F110W and F200LP bands from HST, as well as IR photometry using the *JH* bands from FourStar and I1 and I2 bands from Spitzer. The IR bands are especially helpful in constraining the galaxy mass, since most of the redder light from the bulk of the stars is redshifted out of the optical bands. This spectrophotometry was fit using the spectral energy distribution (SED) fitting code `prospector` (Johnson et al. 2021), primarily in order to correct the shape of the spectrum, which we show in Figure 4. `Prospector` uses Markov Chain Monte Carlo–based stellar population synthesis based on the Python-FSPS framework (Conroy et al. 2009; Foreman-Mackey et al. 2014), as well as the MILES stellar spectral library (Falcón-Barroso et al. 2011) and MIST isochrones (Choi et al. 2016). Our SED modeling of the stellar continuum is described by a delayed-τ parametric star formation history of the form SFR$(t, \tau) \propto (t/\tau)e^{-t/\tau}$, as in

Table 1
Free Parameters Used in `prospector` SED Fitting

Parameter	Description	Priors
z_{obs}	Observed redshift (initialized to mean z from Bleem et al. 2020)	TopHat: $[z-0.001, z+0.001]$
M_{BCG} ($M_\odot$)	Total stellar mass formed	Log_{10} uniform: $[10^9, 10^{13}]$
$\log(Z/Z_\odot)$	Stellar metallicity in log solar units	Clipped normal: $\mu=0.0$, $\sigma=0.3$, range $=[-2.0, 0.5]$
t_{age}	Age of galaxy	TopHat: [0, age of universe at z_{obs}]
τ	e-folding time of star formation history in Gyr	Log_{10} uniform: [0.01, 3.0]
d_2	Optical depth for stellar light attenuation by dust for old stars using extinction curve from Kriek & Conroy (2013, Equation (1)), where observed flux $I = I_0 e^{-d_2}$	TopHat: [0, 20]
Dust ratio	Ratio to convert from dust attenuation optical depth from old stars (d_2) to additional attenuation for young stars	Clipped normal: $\mu=2.3$, $\sigma=0.3$, range $=[0, 3.0]$
δ	Dust index in Kriek & Conroy (2013) extinction curve (Equation (1))	TopHat: $[-2.0, 0.5]$
f_{burst}	Fraction of total stellar mass formed in a recent star formation burst	TopHat: [0, 0.5]
$f_{age,\ burst}$	Time at which burst happens as a fraction of t_{age}	TopHat: [0.1, 1]
σ_v	Velocity smoothing in km s^{-1}	TopHat: [150, 500]
$spec_{norm}$	Spectrum normalization factor to match photometry	Log_{10} uniform: [0.005, 5.0]
$spec_{jitter}$	Part of pixel outlier mixture model to marginalize over poorly modeled noise like residual sky lines or missing absorption lines	TopHat: [1, 10]
$spec_{outlier}$	Multiplicative noise inflation term	TopHat: [0.0001, 1]
(p_1, p_2, p_3)	Continuum calibration (Chebyshev) polynomial	TopHat: $n=3$: $[-0.2/(n+1), 0.2/(n+1)]$

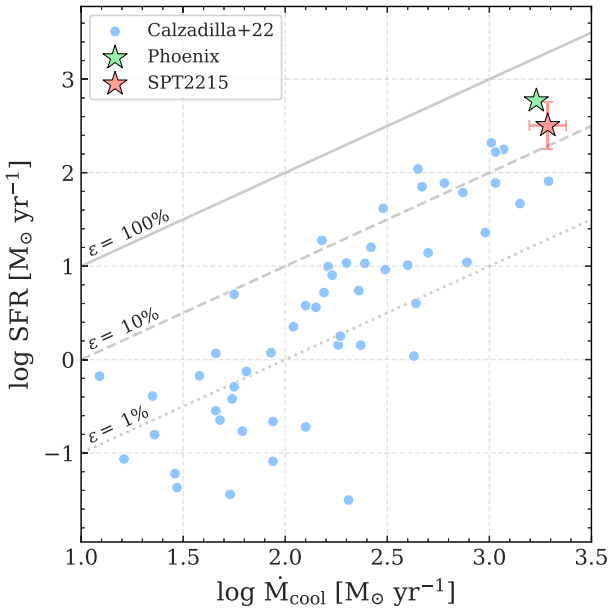

Figure 5. The SFR vs. maximal cooling rate ($\dot{M}_{cool}$, at a radius where $t_{cool}=3$ Gyr) data from Calzadilla et al. (2022) with SPT2215 overlaid, in addition to the Phoenix cluster. Lines of constant cooling efficiency ($\epsilon \equiv SFR/\dot{M}_{cool}$) indicate that over 15% of SPT2215's maximum possible ICM cooling contributes to forming stars.

Khullar et al. (2022), with additional free parameters to capture a burst of recent star formation, as well as the dust attenuation following (Kriek & Conroy 2013, Equations (1)–(3)), with a variable dust index of δ. A description of the priors for each of these parameters may be found in Table 1. To fit only the stellar continuum, we mask the parts of the spectrum associated with potential emission lines from [O II], [O III], and the Balmer series for hydrogen. From these SED fits, we get a best-fit redshift of $z=1.1598\pm0.0005$. We also measure a BCG remnant stellar mass of $\log(M_{BCG}/M_\odot) = (11.77 \pm 0.04)$ with stellar metallicity $\log(Z/Z_\odot) = -0.20 \pm 0.14$, an age of $t=4.5\pm0.5$ Gyr, and a star formation e-folding time of $\tau=1.56\pm0.28$ Gyr. The starburst is estimated to have formed $11\%\pm9\%$ of the remnant stellar mass, starting at $64\%\pm16\%$ of the BCG's age. For the dust extinction associated with the old stellar continuum, we measure $A_{V,s}=0.68\pm0.15$ and an additional gas or young stellar extinction of $A_{V,g}=1.37\pm0.41$.

The best-fit stellar continuum (seen in Figure 4) is subtracted from this flux-calibrated spectrum, and in the residual spectrum, we look for the presence of [O II], which indicates star formation (e.g., Kennicutt 1998; Kewley et al. 2004). We shift the residual observed spectrum to the rest frame and fit a double Gaussian to this [O II] $\lambda\lambda$3726, 2739 doublet, tying the velocity dispersions and wavelengths of the two lines, as well as a straight line to approximate any remaining residual continuum. Our fit in Figure 4 (inset) yields an [O II] flux of $(1.0\pm0.1)\times10^{-15}$ erg s^{-1} cm^{-2}, or a luminosity of 2.6×10^{43} erg s^{-1}. To appropriately calculate an intrinsic (dereddened) flux, we use the extinction measurement for young stars ($A_{V,g}$) cited above, which results in a color excess of $E(B-V)=0.34\pm0.10$, assuming $R_V=4.05$. We thus estimate an intrinsic [O II] flux of $(6.4^{+4.6}_{-2.7})\times10^{-15}$ erg s^{-1} cm^{-2}, or a luminosity of $(4.8^{+3.5}_{-2.0})\times10^{43}$ erg s^{-1}, and use the SFR–$L_{[OII]}$ relation from Kewley et al. (2004) to calculate an SFR of 320^{+230}_{-140} $M_\odot$ yr^{-1}. This SFR is in good agreement with the 600 ± 110 $M_\odot$ yr^{-1} predicted from the empirically calibrated relation between an unobscured SFR and obscured [O II] luminosity from Rosa-González et al. (2002), which can be used when a direct measurement of the extinction is not possible. For robustness, we also tried our SED fitting with the dust attenuation curve of Calzetti et al. (2000) and found a similar extinction and SFR estimate. As a final check, these optically derived SFR estimates are also consistent with the independent UV SFR estimate inferred from the shallow HST data mentioned above. Such a high level of star formation makes SPT2215 stand out among most CC clusters, with only a handful of others exceeding 100 $M_\odot$ yr^{-1}.

Another noteworthy feature of the [O II] detection is the broad line width. With an instrumental broadening-corrected rest-frame width of $\sigma=400\pm50$ km s^{-1}—compared to a typical dispersion of roughly 150 ± 100 km s^{-1} (e.g., Hamer

et al. 2016; Gaspari et al. 2018)—the [O II] emission could be a potential outflow/wind. The total 2D spectrum does not show much structure in the emission in the spatial direction, so a rotation scenario seems unlikely. For comparison, the spatially integrated spectrum of the Phoenix cluster has a line width of $\sigma \sim 350$ km s^{-1} (McDonald et al. 2012). A spatially resolved spectroscopic study of SPT2215 would allow us to understand the origin of this broad, spatially extended emission feature.

4. Discussion

The fact that SPT2215 is a strong CC at such a high redshift gives us a new, unique window into AGN feeding and feedback. In order to investigate the feedback side, we look for the presence of a radio source. We find a faint radio source (see Figure 1, top left panel) with an integrated flux density of 2.0 ± 0.8 mJy at 0.8 GHz detected with the ASKAP radio array (Johnston et al. 2008). This is below the SUMSS (6 mJy beam^{-1} limit) detection limit, and as such, it is not detected in this survey. After k-correction using a spectral index[16] of $\alpha = -0.7$, the 0.8 GHz ASKAP flux corresponds to a 1.4 GHz radio luminosity of 9.3×10^{40} erg s^{-1}. Though our Chandra X-ray data are not deep enough to detect potential cavities and directly calculate an associated cavity power ($P_{\rm cav}$), we can use the 1.4 GHz radio luminosity and the scaling relation from Cavagnolo et al. (2010) to estimate $\log (P_{\rm cav}/10^{42}$ erg s$^{-1}) = 2.6 \pm 0.3$ (stat.)$\pm$ 0.8 (int. scatter). From our X-ray analysis, we also estimate a cooling luminosity of $L_{\rm cool} = (3.7 \pm 0.1) \times 10^{45}$ erg s^{-1}, which is the bolometric (0.01–100 keV) X-ray luminosity measured within a radius of 116 kpc, where the $t_{\rm cool}$ profile reaches 3 Gyr. These measurements yield a ratio of $\log(P_{\rm cav}/L_{\rm cool}) = -1.0 \pm 0.8$ (where the uncertainty is dominated by the scatter in the $P_{\rm cav}$–$L_{1.4\ \rm GHz}$ relation), which suggests that the ICM cooling is overwhelming the AGN feedback in this system by an order of magnitude. This measured $P_{\rm cav}/L_{\rm cool}$ ratio is suggestive of a strong imbalance between heating and cooling but ultimately consistent with the large amount of scatter found in $P_{\rm cav}/L_{\rm cool}$ as a function of redshift (Ruppin et al. 2022).

With a massive CC and $P_{\rm cav}/L_{\rm cool} \approx 0.1$, it may be no surprise that we measure such a high SFR. Perhaps more noteworthy is the fact that, compared to its maximal cooling rate of $\dot{M}_{\rm cool} \sim 1900\ M_\odot$ yr^{-1}, we calculate a cooling conversion efficiency of $\epsilon_{\rm cool} \equiv {\rm SFR}/\dot{M}_{\rm cool} = 17\% \pm 10\%$. It may be argued that the radius where we measure $L_{\rm cool}$ and $\dot{M}_{\rm cool}$ is somewhat arbitrary, so for comparison, we calculate these at a radius of $\sim$20 kpc, where we actually observe the cooling filaments (Figure 1, lower left panel). At this smaller radius, $t_{\rm cool,\ 20} \approx 0.3$ Gyr, $\dot{M}_{\rm cool,\ 20} = 610 \pm 220\ M_\odot$ yr^{-1}, and $L_{\rm cool,\ 20} = (8.4 \pm 0.5) \times 10^{44}$ erg s^{-1}, and the resulting cooling conversion efficiency is much higher at $\epsilon_{\rm cool,\ 20} = 52\% \pm 36\%$. In most low-redshift systems, cooling is suppressed by about 2 orders of magnitude, on average, with $\epsilon_{\rm cool} \sim 1\%$. However, Calzadilla et al. (2022) found that $\epsilon_{\rm cool}$ scales directly with $\dot{M}_{\rm cool}$, as shown in Figure 5 (see also Fogarty et al. 2017; McDonald et al. 2018). The high value of $\epsilon_{\rm cool}$ measured in SPT2215 is consistent with this trend toward increasingly efficient cooling in the strongest CCs, though the reason for this trend is still not understood (Calzadilla et al. 2022).

[16] Where the flux density S_ν scales with frequency as $S_\nu \propto \nu^\alpha$.

The simplest explanation for the high SFR in SPT2215 is that cooling is exceeding heating in this system. This is supported by the observation that the cooling luminosity is a factor of 2 higher than the jet power, which ought to lead to a large residual cooling flow. However, the jet power here is being constrained via the radio luminosity, which can vary by factors of several on $\sim$10 yr timescales (e.g., Dutson et al. 2014), which makes it difficult to reliably connect it to the time-averaged jet power. With deeper observations, we could detect or put limits on the presence of X-ray cavities, which would provide an estimate of the long-term jet power output, providing a better basis for comparison to the cooling luminosity.

Regardless of what the true $P_{\rm cav}/L_{\rm cool}$ ratio is, a significant power imbalance in one system is unlikely to explain the overall trend toward increasingly efficient cooling in the most massive CCs, such as SPT2215. An alternative explanation relates to the idea that CCs are in a stable cycle between cooling and feedback. If accretion of cold gas onto an SMBH can trigger jets, which, in turn, can lift low-entropy gas to larger radii in the cluster, then cooling will be suppressed for roughly a rise and freefall time before the cycle starts anew (e.g., Prasad et al. 2020). If this system is like a harmonic oscillator between cooling cycles, then the frequency of oscillation will depend on the depth of the potential. That is, the low-entropy gas will return to the cluster center much faster in a cluster with a deeper central potential than in a cluster with a shallow central potential. If this freefall timescale is shorter than the timescale for consuming the reservoir of cold, dense gas via star formation, then that reservoir will constantly be replenished, leading to higher average SFRs compared to systems where star formation can cycle between on and off. This is a hypothesis that we can and intend to test via the combination of state-of-the-art simulations and data for a large variety of CC clusters (e.g., Calzadilla et al. 2022).

Object SPT2215 is similar to many of the most well-studied extreme CC clusters at low redshifts, but it is rare in that we observe it at such high redshift. As a point of contrast, it was recently argued that the even higher redshift ($z = 1.7$) galaxy cluster SpARCS1049 was rapidly forming stars (SFR of $\sim$860 $M_\odot$ yr^{-1}) from a cooling flow facilitated by a recent dynamical encounter that physically separated the low-entropy gas from the central galaxy, allowing for cooling in the absence of local feedback (Webb et al. 2015; Hlavacek-Larrondo et al. 2020). Over time, SpARCS1049 may be expected to relax, leading to suppression of the cooling flow once it is aligned with and directed toward the BCG and central SMBH. In this sense, SPT2215 may be a potential intermediate step between a system like SpARCS1049 and other relaxed low-redshift systems, as the ICM cooling is centered on a BCG and there are signs of weak radio emission, possibly from a very recently activated AGN.

On the other hand, the high level of relaxedness in SPT2215 implies that, if a dynamical interaction triggered some initial cooling episode, it likely happened long ago. More realistically, SPT2215 and SpARCS1049 may represent two distinct avenues to rapid cooling of the ICM, either via a strong dynamical encounter that physically separates low-entropy gas from the source of feedback or via a potential so deep that the freefall time of the uplifted gas is shorter than the consumption time of the cold reservoir. Instead, SPT2215 seems to be a high-z analog of the Phoenix cluster, not only in how intensely

star-forming it is but also in how massive and relaxed it is. Our SED fitting results in Section 3.2 suggest that the BCG itself is exceptionally massive, with a surviving stellar mass of $M_{\rm BCG} = (5.9 \pm 0.6) \times 10^{11}\ M_{\odot}$. This inferred mass is consistent with that predicted by the scaling relations between stellar mass and the combination of Spitzer magnitudes and g–r colors found in Zhu et al. (2010, Equations (6)–(7)). Such an extraordinary mass at this redshift implies that SPT2215 may have had a head start in its accretion history, allowing it to grow extremely quickly. This is a trait that SPT2215 shares with the Phoenix cluster, which is also exceptionally massive and shows no sign of a recent merger, indicating rapid, early growth. Why such a rapid growth followed by a period of relaxedness ought to lead to overcooling of the core remains an open question, but it seems unlikely to be a coincidence.

5. Summary

Object SPT2215 is a unique cluster in that it is the most distant yet found of a remarkable set of extreme cool cores. Using multiwavelength imaging and spectral observations, we have demonstrated that this system consists of a strongly cooling X-ray core (at a radius of 10 kpc, the central entropy and cooling time reach $\sim$20 keV cm^2 and 200 Myr, respectively, and the maximal ICM cooling rate at a radius where the cooling time reaches 3 Gyr is $\dot{M}_{\rm cool} \sim 1900\ M_{\odot}\ {\rm yr}^{-1}$). This cool core is at the center of a dynamically relaxed cluster, which appears to be fueling a massive starburst ($320^{+230}_{-140}\ M_{\odot}\ {\rm yr}^{-1}$) in a highly evolved central giant elliptical galaxy. Further X-ray observations (A. Mantz et al. 2023, in preparation) will allow more precise thermodynamic profile modeling, measurement of the gas fraction, and further constraints on cosmological models. Our shallow HST data already reveal hints of complex star-forming filaments, which will benefit from deeper observations with HST or perhaps even the JWST/NIRSpec IFU in order to more precisely measure SFRs and reddening and further understand the underlying process of cluster star formation in a previously untapped redshift regime.

Based on observations made with the NASA/ESA Hubble Space Telescope, obtained at the Space Telescope Science Institute, which is operated by the Association of Universities for Research in Astronomy, Inc., under NASA contract NAS 5-26555. These observations are associated with program numbers 15307, 15661, and 16001. The authors acknowledge support from programs HST-GO-15307.008-A, HST-GO-15661.001, and HST-GO-16001.002, provided through grants from the STScI under NASA contract NAS5-26555. The authors also acknowledge additional financial support for this work provided by the National Aeronautics and Space Administration through Chandra Award No. GO0-21124A issued by the Chandra X-ray Center, which is operated by the Smithsonian Astrophysical Observatory for and on behalf of the National Aeronautics Space Administration under contract NAS8-03060. The South Pole Telescope program is supported by the National Science Foundation (NSF) through grants PLR-1248097 and OPP-1852617. Partial support is also provided by NSF Physics Frontier Center grant PHY-1125897 to the Kavli Institute of Cosmological Physics at the University of Chicago, the Kavli Foundation, and the Gordon and Betty Moore Foundation through grant GBMF#947 to the University of Chicago. Argonne National Laboratory's work was supported by the U.S. Department of Energy, Office of Science, Office of High Energy Physics, under contract DE-AC02-06CH11357. This paper used data gathered with the 6.5 m Magellan Telescopes located at Las Campanas Observatory, Chile. We thank the staff of Las Campanas for their dedicated service, which has made these observations possible. The scientific results reported in this paper are based on observations made by the Chandra X-ray Observatory, and this research has made use of software provided by the Chandra X-ray Center (CXC) in the application package CIAO. M.S.C. acknowledges support from NASA Headquarters under Future Investigators in NASA Earth and Space Science and Technology (FINESST) award 20-Astro20-0037. A.A.S. acknowledges support from NSF award 2109035. G.M. acknowledges funding from the European Union's Horizon 2020 research and innovation program under Marie Sklodowska-Curie grant agreement No. MARACHAS—DLV-896778.

Facilities: CXO, HST, NSF/US Department of Energy 10 m South Pole Telescope (SPTpol), Magellan 6.5 m telescopes (Clay/LDSS3C, Clay/PISCO, Baade/FourStar).

Software: astropy (Astropy Collaboration et al. 2013), numpy (Harris et al. 2020), scipy (Virtanen et al. 2020), pandas (Reback et al. 2022), CIAO (Fruscione et al. 2006), XSPEC (Arnaud 1996), prospector (Johnson et al. 2021), python-FSPS (Foreman-Mackey et al. 2014), SEDpy (Johnson 2021), matplotlib (Hunter 2007), seaborn (Waskom 2021), jupyter/IPython Notebooks (Kluyver et al. 2016), SAOImage DS9 (Joye & Mandel 2003), pyRAF (Science Software Branch at STScI 2012), SExtractor (Bertin & Arnouts 1996).

ORCID iDs

Michael S. Calzadilla https://orcid.org/0000-0002-2238-2105
Lindsey E. Bleem https://orcid.org/0000-0001-7665-5079
Michael McDonald https://orcid.org/0000-0001-5226-8349
Michael D. Gladders https://orcid.org/0000-0003-1370-5010
Adam B. Mantz https://orcid.org/0000-0002-8031-1217
Steven W. Allen https://orcid.org/0000-0003-0667-5941
Matthew B. Bayliss https://orcid.org/0000-0003-1074-4807
Anna-Christina Eilers https://orcid.org/0000-0003-2895-6218
Benjamin Floyd https://orcid.org/0000-0003-4175-571X
Julie Hlavacek-Larrondo https://orcid.org/0000-0001-7271-7340
Gourav Khullar https://orcid.org/0000-0002-3475-7648
Keunho J. Kim https://orcid.org/0000-0001-6505-0293
Guillaume Mahler https://orcid.org/0000-0003-3266-2001
Keren Sharon https://orcid.org/0000-0002-7559-0864
Taweewat Somboonpanyakul https://orcid.org/0000-0003-3521-3631
Brian Stalder https://orcid.org/0000-0003-0973-4900
Antony A. Stark https://orcid.org/0000-0002-2718-9996

References

Abbott, T. M. C., Abdalla, F. B., Allam, S., et al. 2018, ApJS, 239, 18
Allen, S. W. 1995, MNRAS, 276, 947
Anders, E., & Grevesse, N. 1989, GeCoA, 53, 197
Arnaud, K. A. 1996, in ASP Conf. Ser. 101, Astronomical Data Analysis Software and Systems V, ed. George H. Jacoby & J. Barnes (San Francisco, CA: ASP), 17
Ashby, M. L. N., Stern, D., Brodwin, M., et al. 2009, ApJ, 701, 428
Astropy Collaboration, Robitaille, T. P., Tollerud, E. J., et al. 2013, A&A, 558, A33
Bayliss, M. B., Ruel, J., Stubbs, C. W., et al. 2016, ApJS, 227, 3
Bertin, E., & Arnouts, S. 1996, A&AS, 117, 393
Bleem, L. E., Bocquet, S., Stalder, B., et al. 2020, ApJS, 247, 25

Bleem, L. E., Stalder, B., Brodwin, M., et al. 2015, ApJS, 216, 20
Bleem, L. E., Stalder, B., de Haan, T., et al. 2015, ApJS, 216, 27
Calzadilla, M. S., McDonald, M., Bayliss, M., et al. 2019, ApJL, 887, L17
Calzadilla, M. S., McDonald, M., Donahue, M., et al. 2022, ApJ, 940, 140
Calzetti, D., Armus, L., Bohlin, R. C., et al. 2000, ApJ, 533, 682
Cavagnolo, K. W., Donahue, M., Voit, G. M., et al. 2008, ApJL, 683, L107
Cavagnolo, K. W., McNamara, B. R., Nulsen, P. E. J., et al. 2010, ApJ, 720, 1066
Choi, J., Dotter, A., Conroy, C., et al. 2016, ApJ, 823, 102
Conroy, C., Gunn, J. E., & White, M. 2009, ApJ, 699, 486
Crawford, C. S., Allen, S. W., Ebeling, H., et al. 1999, MNRAS, 306, 857
D'Onghia, E., Sommer-Larsen, J., Romeo, A. D., et al. 2005, ApJL, 630, L109
Donahue, M., Connor, T., Fogarty, K., et al. 2015, ApJ, 805, 177
Donahue, M., & Voit, G. M. 2022, PhR, 973, 1
Dutson, K. L., Edge, A. C., Hinton, J. A., et al. 2014, MNRAS, 442, 2048
Fabian, A. C. 1994, ARA&A, 32, 277
Fabian, A. C. 2012, ARA&A, 50, 455
Falcón-Barroso, J., Sánchez-Blázquez, P., Vazdekis, A., et al. 2011, A&A, 532, A95
Fogarty, K., Postman, M., Larson, R., et al. 2017, ApJ, 846, 103
Foreman-Mackey, D., Sick, J., & Johnson, B. 2014, python-fsps: Python bindings to FSPS v0.1.1, Zenodo doi:10.5281/zenodo.12157
Fruscione, A., McDowell, J. C., Allen, G. E., et al. 2006, Proc. SPIE, 6270, 62701V
Gaspari, M., McDonald, M., Hamer, S. L., et al. 2018, ApJ, 854, 167
Gaspari, M., Tombesi, F., & Cappi, M. 2020, NatAs, 4, 10
Hamer, S. L., Edge, A. C., Swinbank, A. M., et al. 2016, MNRAS, 460, 1758
Harris, C. R., Millman, K. J., van der Walt, S. J., et al. 2020, Natur, 585, 357
High, F. W., Stubbs, C. W., Rest, A., et al. 2009, AJ, 138, 110
Hilton, M., Sifón, C., Naess, S., et al. 2021, ApJS, 253, 3
Hlavacek-Larrondo, J., Fabian, A. C., Edge, A. C., et al. 2013, MNRAS, 431, 1638
Hlavacek-Larrondo, J., McDonald, M., Benson, B. A., et al. 2015, ApJ, 805, 35
Hlavacek-Larrondo, J., Rhea, C. L., Webb, T., et al. 2020, ApJL, 898, L50
Hudson, D. S., Mittal, R., Reiprich, T. H., et al. 2010, A&A, 513, A37
Hunter, J. D. 2007, CSE, 9, 90
Johnson, B. D., Leja, J., Conroy, C., & Speagle, J. S. 2021, bd-j/prospector: prospector v1.0.0, Zenodo doi:10.5281/zenodo.4586953
Johnson, B. D., Leja, J., Conroy, C., et al. 2021, ApJS, 254, 22
Johnston, S., Taylor, R., Bailes, M., et al. 2008, ExA, 22, 151
Johnstone, R. M., Fabian, A. C., & Nulsen, P. E. J. 1987, MNRAS, 224, 75
Jones, L. R., Ponman, T. J., Horton, A., et al. 2003, MNRAS, 343, 627
Joye, W. A., & Mandel, E. 2003, in ASP Conf. Ser. 295, Astronomical Data Analysis Software and Systems XII, ed. H. E. Payne, R. I. Jedrzejewski, & R. N. Hook (San Francisco, CA: ASP), 489
Kalberla, P. M. W., Burton, W. B., Hartmann, D., et al. 2005, A&A, 440, 775
Kennicutt, R. C. 1998, ARA&A, 36, 189
Kewley, L. J., Geller, M. J., & Jansen, R. A. 2004, AJ, 127, 2002
Khullar, G., Bayliss, M. B., Gladders, M. D., et al. 2022, ApJ, 934, 177
Khullar, G., Bleem, L. E., Bayliss, M. B., et al. 2019, ApJ, 870, 7
Kluyver, T., Ragan-Kelley, B., Pérez, F., et al. 2016, in Positioning and Power in Academic Publishing: Players, Agents and Agendas, ed. F. Loizides & B. Schmidt (Amsterdam: IOS Press), 87
Kriek, M., & Conroy, C. 2013, ApJL, 775, L16
Liu, A., Bulbul, E., Ghirardini, V., et al. 2022, A&A, 661, A2
Mantz, A. B., Allen, S. W., Morris, R. G., et al. 2015, MNRAS, 449, 199
Mantz, A. B., Morris, R. G., Allen, S. W., et al. 2022, MNRAS, 510, 131
McDonald, M., Allen, S. W., Bayliss, M., et al. 2017, ApJ, 843, 28
McDonald, M., Bayliss, M., Benson, B. A., et al. 2012, Natur, 488, 349
McDonald, M., Benson, B. A., Vikhlinin, A., et al. 2013, ApJ, 774, 23
McDonald, M., Gaspari, M., McNamara, B. R., et al. 2018, ApJ, 858, 45
McDonald, M., Veilleux, S., Rupke, D. S. N., et al. 2010, ApJ, 721, 1262
McNamara, B. R., & Nulsen, P. E. J. 2007, ARA&A, 45, 117
McNamara, B. R., & Nulsen, P. E. J. 2012, NJPh, 14, 055023
McNamara, B. R., & O'Connell, R. W. 1989, AJ, 98, 2018
Miknaitis, G., Pignata, G., Rest, A., et al. 2007, ApJ, 666, 674
Milosavljević, M., Miller, C. J., Furlanetto, S. R., et al. 2006, ApJL, 637, L9
Morrison, R., & McCammon, D. 1983, ApJ, 270, 119
O'Dea, C. P., Baum, S. A., Privon, G., et al. 2008, ApJ, 681, 1035
Persson, S. E., Murphy, D. C., Smee, S., et al. 2013, PASP, 125, 654
Planck Collaboration, Ade, P. A. R., Aghanim, N., et al. 2016, A&A, 594, A27
Prasad, D., Sharma, P., Babul, A., et al. 2020, MNRAS, 495, 594
Rafferty, D. A., McNamara, B. R., Nulsen, P. E. J., et al. 2006, ApJ, 652, 216
Reback, J., Jbrockmendel, A., McKinney, W., et al. 2022, pandas-dev/pandas: Pandas 1.4.4, Zenodo, doi:10.5281/zenodo.7037953
Rosa-González, D., Terlevich, E., & Terlevich, R. 2002, MNRAS, 332, 283
Ruppin, F., McDonald, M., Bleem, L. E., et al. 2021, ApJ, 918, 43
Ruppin, F., McDonald, M., Hlavacek-Larrondo, J., et al. 2022, arXiv:2207.13351
Science Software Branch at STScI 2012, PyRAF: Python alternative for IRAF, Astrophysics Source Code Library, ascl:1207.011
Skrutskie, M. F., Cutri, R. M., Stiening, R., et al. 2006, AJ, 131, 1163
Smith, R. K., Brickhouse, N. S., Liedahl, D. A., et al. 2001, ApJL, 556, L91
Somboonpanyakul, T., McDonald, M., Noble, A., et al. 2022, AJ, 163, 146
Stalder, B., Stark, A. A., Amato, S. M., et al. 2014, Proc. SPIE, 9147, 91473Y
Sutherland, R. S., & Dopita, M. A. 1993, ApJS, 88, 253
Tozzi, P., & Norman, C. 2001, ApJ, 546, 63
van den Bosch, F. C., Yang, X., Mo, H. J., et al. 2007, MNRAS, 376, 841
Vanderlinde, K., Crawford, T. M., de Haan, T., et al. 2010, ApJ, 722, 1180
Vikhlinin, A., Kravtsov, A., Forman, W., et al. 2006, ApJ, 640, 691
Virtanen, P., Gommers, R., Oliphant, T. E., et al. 2020, NatMe, 17, 261
Waskom, M. L. 2021, JOSS, 6, 60
Webb, T., Noble, A., DeGroot, A., et al. 2015, ApJ, 809, 173
Zhu, Y.-N., Wu, H., Li, H.-N., et al. 2010, RAA, 10, 329